The International Journal of Advanced Manufacturing Technology (2019) 102:2119–2132
https://doi.org/10.1007/s00170-018-03283-9

ORIGINAL ARTICLE

Material extrusion-based additive manufacturing of structurally controlled poly(lactic acid)/carbon nanotube nanocomposites

Ali Nadernezhad[1] · Serkan Unal[2] · Navid Khani[1] · Bahattin Koc[1,2]

Received: 11 May 2018 / Accepted: 28 December 2018 / Published online: 21 January 2019

Abstract

The mesostructure of additively manufactured nanocomposite parts can be tailored by the manipulation of process parameters to improve the properties of the final part. The effects of contributing process parameters and their interactions must be identified to be able to tune the properties of additively manufactured (3D-printed) nanocomposites based on their intended applications. Herein, we present the characterization of the effect of three major building parameters, namely layer thickness, infill percentage, and infill pattern, on mechanical and thermal properties of 3D-printed poly(lactic acid) (PLA)/carbon nanotube (CNT) nanocomposites. The characterization of printed parts showed that increasing layer thickness had a deteriorating effect on the mechanical properties regardless of the CNT concentration; however, the Young's modulus and tensile strength of parts were improved by increasing the CNT content in the same design of mesostructure. Moreover, the thermomechanical analysis showed that the residual thermal stresses of 3D-printed nanocomposites increased by increasing the layer thickness. Furthermore, it was shown that decreasing infill percentage resulted in a non-linear reduction of stiffness, strength, and dimensional stability. Moreover, a honeycomb-shaped infill pattern was introduced for the manufacturing of parts, which has shown more isotropic mechanical properties. The contributions of CNTs in enhancing mechanical properties of 3D-printed nanocomposites were investigated, by considering the induced reinforcing effects as well as the alteration of the crystallization behavior of PLA.

Keywords 3D printing · PLA/CNT nanocomposites · Process parameters · Mechanical characterization

1 Introduction

The demand for additive manufacturing (AM) has been growing rapidly [1], mainly due to unrivaled design freedom and ability to directly manufacture highly complex and customized geometries with various materials. Material extrusion-based AM, also called 3D printing, is one of the most commonly used AM technologies, and the commercialization of 3D printers led to its extensive utilization in both prototyping and manufacturing of functional end-use products. However, the mechanical durability of parts manufactured by conventional material extrusion-based AM is often limited, mainly due to the inherent poor mechanical properties of 3D-printed plastics or because of structural inhomogeneities and imperfections induced during the process [2]. Several studies have been devoted to identifying the effect of key process parameters on the mechanical properties of 3D-printed parts [3–9] and optimization of interaction effects [4, 10–13]. However, optimizing process parameters by itself may not be enough to achieve the intended printed part properties because of the limited properties of the polymeric materials used for 3D printing.

Polymeric nanocomposite materials offer improved mechanical and thermal properties in 3D-printed parts, for which different nanoparticles have been used to provide multiple functionalities [14, 15]. In this regard, 3D printing of various polymeric nanocomposites was investigated in a few studies, including ABS/graphene [16–18], ABS/nano-clay [19], ABS/CNT [20], yarn/CNT [21], PBT/CNT [22], PEEK/CNT [23], polyamide/graphene [24], PLA/graphene [25–27], and PLA/CNT [28] nanocomposites. Although the incorporation of nanoparticles within a polymer matrix often results in enhanced mechanical properties, the inherent anisotropy [8, 29] of 3D-printed parts and the inducing factors, such as part

✉ Bahattin Koc
bahattinkoc@sabanciuniv.edu

[1] Faculty of Engineering and Natural Sciences, Sabanci University, Istanbul, Turkey

[2] Sabanci University Integrated Manufacturing Technologies Research and Application Center, Istanbul, Turkey

temperature, raster orientation, bead width, and air gap, should be carefully considered in the design and manufacturing steps. In other words, the presence of nanoparticles within the polymer matrix may not necessarily induce a noteworthy enhancement in mechanical properties. An imprecise combination of materials for this purpose might even result in the deterioration of mechanical properties of 3D-printed parts depending on the characteristics of selected materials and process parameters [16]. The preparation and characterization of polymeric nanocomposites based on PLA and carbon nanotubes (CNTs) have been reported in the literature [30, 31]. It is well-established that the inclusion of CNTs within the PLA matrix offers enhanced crystallization kinetics and improved tensile stiffness and thermal stability based on the characterization of solution cast or injection molded test specimens. However, considering that PLA as one of the most commonly used polymers in extrusion-based 3D printing, there are a few studies available in the literature, in which a systematic exploration of process parameters for 3D printing of PLA/CNT nanocomposites has been mostly neglected [28, 32]. Patanwala et al. reported about the preparation and characterization of PLA/CNT nanocomposites for 3D printing and performed an in-depth characterization on the flow behavior of nanocomposites during extrusion; however, their study was limited to the investigation of printing flow rate for a fixed printing gap and nozzle diameter [28]. The influence of possible interactions between intrinsic properties of PLA/CNT nanocomposites and 3D printing process parameters on the properties of final 3D-printed parts is yet to be characterized.

The process parameters in 3D printing play a significant role in determining the mechanical and thermal properties of final parts. Among them, nozzle diameter, layer thickness, raster orientation, infill percentage, and extrusion temperature are the most influential parameters of the process [14, 15]. Close control and optimization of these parameters will enable the tuning and improvement of final properties of 3D-printed parts based on requirements for a given application. Other factors, such as the time and cost of production, should also be considered to mimic the realistic process conditions [12].

In this study, we present a systematic approach on the characterization of thermal and mechanical properties of PLA/CNT nanocomposites under realistic 3D printing conditions, specifically in the case of density (infill percentage), which is one of the most critical parameters in determination of the mechanical durability of final printed parts. Although the infill percentage has generally been considered as to be 100% in most of the previous studies, the consideration of lower infill percentages in 3D printing will result in the reduction of weight, cost, and production time. This issue has been addressed in a number of studies focused on the mutual effects of infill density and orientation on mechanical strength [5, 33–37] and production cost [33] of additively manufactured cellular structures. It was demonstrated that decreasing the infill density will result in deterioration of the mechanical properties of PLA [35, 36], ABS [5, 33, 34], and polypropylene [37] parts. Moreover, it was observed that the production cost could be tuned by adjusting the infill density, in such a way that the percentage loss in mechanical strength of the additively manufactured parts was reasonably preserved in an exchange with a significant saving in the production cost [33]. However, the effect of infill density in 3D-printed parts from polymer nanocomposite has been mostly neglected. While the process parameters are the sole factors to determine the mechanical properties of the 3D-printed pure plastics, the intrinsic properties of polymer nanocomposites can be adjusted by controlling the reinforcing nanoparticles, which brings more freedom in selection of the 3D printing process parameters in the production of mechanically durable cellular structures. In addition to the infill parameters, several other important parameters, such as the effect of infill pattern and the layer thickness on thermal and mechanical properties of 3D-printed nanocomposites, were also studied.

2 Experimental

2.1 Materials and preparation of nanocomposites

PLA was purchased from NatureWorks LLC (Ingeo 4043D, NatureWorks, UK). Multiwall CNTs were acquired from Nanocyl S.A. (Nanocyl NC7000 nanotubes, Belgium) with the average diameter of 9.5 nm and 1.5-μm length and used as received (degree of purity > 90%). PLA/CNT nanocomposites were prepared by melt compounding process using a twin screw extruder (Zamak Mercator, Poland). Polymer powders were dried at 40 °C in vacuo for 6 h before compounding with CNTs. The temperature profile of heated zones from feeding hopper to the die was set to 45, 177, 185, 190, 195, 199, 199, and 191 °C with a constant screw rotation speed of 450 rpm. Various PLA/CNT nanocomposites with CNT contents of 0.1, 0.3, 0.5, and 1.0 wt% were prepared. Neat PLA was extruded under the same conditions to produce control samples with the same thermo-mechanical history. Our preliminary studies (data not shown here) revealed that further increase in CNTs concentration will negatively affect the state of filler dispersion and will also induce brittle fracture behavior. Hence, the filler loading was limited to 1.0 wt% to have a better understanding of the mutual interactions between process and material related properties in the mechanical behavior of cellular structures.

The melt-compounded nanocomposites were injection molded by DSM Xplore 12-mL laboratory injection-molding machine using the preheated transfer cylinder to obtain the standard tensile test dumbbell shape samples according to ISO 527-2 type 1BA. The injection and holding

pressures were set to 10 bars. Melt temperature and mold temperatures were 220 and 30 °C, respectively.

PLA/CNT nanocomposite pellets were used to produce filaments by using an in-house developed single screw extruder. Extrusion was performed at a constant rotation speed of 75 rpm, and the temperature of the barrel and die set to 168 and 180 °C, respectively. Filaments were air cooled after extrusion, while the diameter was kept at 1.95 ± 0.05 mm by adjusting the winder speed.

2.2 3D printing and path planning

A path planning algorithm was developed for the fabrication of 3D-printed nanocomposite structures using Rhinoscript (Rhinoceros 5.0, Robert McNeel & Associates, USA) with specific building parameters and geometries for tensile testing (dumbbell shape) and thermomechanical analysis (TMA) (cuboid shape). The developed path planning algorithm was used to generate CNC-based instructions, which have overridden the default settings of the commercial 3D printer by changing the input filament diameter and the corresponding extrusion flow rates. In this way, fully customizable path planning instructions were generated for the extruded composite filaments. Three major building parameters were considered and studied as key variables during path planning: the layer thickness, infill density, and infill pattern. Table 1 lists the seven different designs that were employed in this study. The path plans were used to generate G-codes by considering the specifications of each design. The samples for tensile and thermo-mechanical testing were 3D printed by the generated G-codes using Ultimaker 2 (Ultimaker, Netherlands) desktop 3D printer on the standard glass substrate. The mesostructure of each infill pattern of path plans is shown in Fig. 1. Each design was used for the fabrication of testing samples from neat PLA and PLA/CNT nanocomposites with different CNT concentrations. The build platform temperature and printing speed were set to 60 °C and 30 mm/s, respectively.

Table 1 Path planning parameters for the fabrication of nanocomposite samples for mechanical testing

Design no.	Layer thickness (mm)	Raster orientation	Infill density (%)
1	0.1	−45/+45	60
2	0.2	−45/+45	60
3	0.3	−45/+45	60
4	0.2	−45/+45	40
5	0.2	−45/+45	80
6	0.2	0/90	60
7	0.2	Honeycomb	60

All the samples were 3D printed with 0.4-mm nozzle diameter. Only one sample was 3D printed during each build cycle to minimize the difference between thermal histories of specimens.

2.3 Characterization

The PLA/CNT nanocomposite samples directly cut from injection molded or 3D printed were thermally characterized in triplicates by differential scanning calorimetry (DSC, Q2000 TA Instruments, USA) using heating-cooling-heating cycles from − 25 to 250 °C at a heating and cooling rate of 10 °C/min under nitrogen atmosphere. The samples were isothermally heated at the end of each heating/cooling cycle for 2 min to reach the equilibrium temperature condition. The percent crystallinity (X_c) of each sample with a known weight fraction of PLA (ϕ) was calculated by using the enthalpy of melting (ΔH_m) and enthalpy of cold crystallization (ΔH_c) during the first heating cycle to interpret mechanical test results considering the effect of the thermal history [38]. The heat of fusion of 100% crystalline PLA (ΔH_m^0) was considered as 93.1 J/g [39]. Glass transition temperature (T_g) and cold crystallization peak temperature (T_{cc}) were reported from the second heating cycle. The microstructure of PLA/CNT nanocomposites was investigated using Zeiss Leo Supra VP 35 (Carl Zeiss AG, Germany) field emission scanning electron microscope using 4.0 keV. The cryo-fracture surfaces were produced by fracturing the bar-shaped injection molded samples in liquid nitrogen. The mechanical properties of nanocomposites were determined using a Zwick-Roell Z100 universal testing machine (Germany) using 10-kN crosshead. For this purpose, the dumbbell-shape samples of compounded nanocomposites were produced by injection molding using Netstal 600 H-110 (Netstal, Switzerland) according to dimensions in the ISO 527-2 standard type 1BA. The same-shaped 3D-printed samples were also prepared according to the same standard. Tensile testing conditions were set according to the ISO 527-2 standard, including the test speed of 1 mm/min, a gauge length of 25 mm, and the initial distance between grips equal to 58 mm. At least five replicates of each sample were tested for tensile measurements.

The TMA of 3D-printed nanocomposites was performed by Mettler-Toledo TMA/SDTA 2+ LN/600 using a ball-point probe in compression mode according to ASTM E831-06. The cuboid samples were produced by 3D printing with dimensions ($W \times L \times H$) set to $5 \times 10 \times 4$ mm^3 to accommodate the TMA. The temperature scans were performed in the range of 0–130 °C with a heating rate of 10 °C/min at a constant force of 0.01 N, and change in sample dimension in the z-axis of 3D printing (along h) was measured. All the TMA measurements were performed in triplicates.

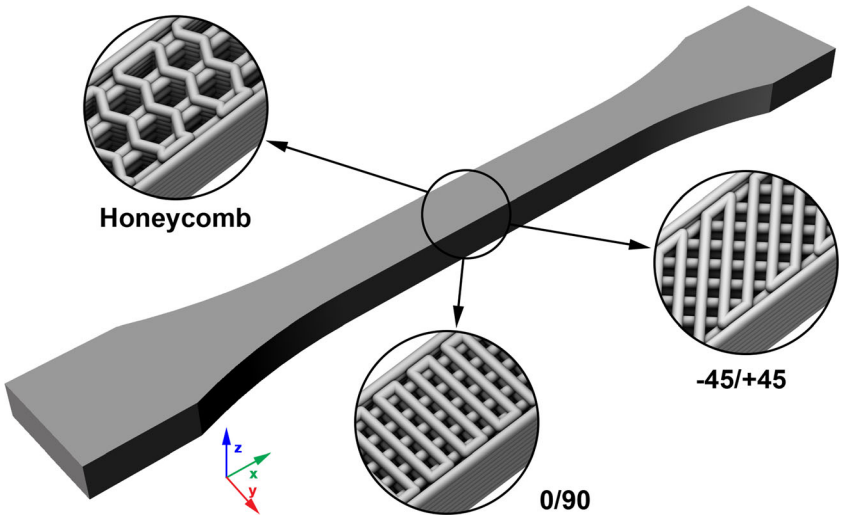

Fig. 1 Mesostructure of samples for different infill patterns generated in path planning

3 Results and discussion

3.1 Melt compounded PLA/CNT nanocomposites

Thermal and mechanical characteristics of melt compounded nanocomposite have a direct impact on the properties of the 3D-printed product. In order to provide an overview about the bulk mechanical properties and also to benchmark the effect of the CNT content in different composites against the pure PLA, tensile testing was performed, and the corresponding results are provided in this section. It should be noted that since PLA is a semi-crystalline polymer, the amount of the crystalline portion has a significant effect on the subsequent mechanical properties. The percent crystallinity of PLA and its nanocomposites strongly depend on the thermal history. Moreover, the inclusion of CNTs will potentially change the crystallization kinetics of the nanocomposites and depending on the concentration of the fillers; a different crystallization behavior might be expected. All being said, performing a thermal characterization on the melt compounded samples would provide some structural insights into the composite systems. The DSC thermographs of neat PLA and PLA/CNT nanocomposites are presented in Fig. 2, and the results of the DSC analysis are provided in Table 2. The incorporation of CNTs into the PLA matrix resulted in decreased cold crystallization temperature (T_{cc}). This can be attributed to the effect of CNTs as nucleating agents in PLA/CNT nanocomposites, by promoting heterogeneous nucleation within the matrix, which in turn resulted in lower energy consumption required to reach the critical stability value for crystal growth [40, 41]. It should be noted that the T_{cc} of PLA/CNT nanocomposites decreased upon the incorporation of lower CNT content (0.1 wt%) and then gradually increased with increasing CNT content. The observed re-increase in T_{cc} could be related to increased restriction of chains' mobility in the PLA matrix and decreased the plasticizing effect of nanofillers by increasing their concentration [40]; yet, the T_{cc} of PLA/CNT nanocomposites was lower than neat PLA at all CNT contents. The presence of CNTs in the PLA matrix also resulted in double endothermic melting peaks, differently from a single melting peak in neat PLA. This behavior might be due to the formation of two separate crystal phases, namely α and α', resulting in a complex melting-recrystallization-remelting behavior in the presence of nano-fillers as also reported earlier in the literature [42]. The low-melting (L) and high-melting (H) peaks in double melting endotherms were observed at the similar temperature values for all nanocomposites with CNT contents below 1 wt%. However, increased CNT content to 1 wt% resulted in a slight shift of L and H peak temperatures and a significant decrease in the ratio between the peak area of peak H to that of peak L. According to the melt recrystallization model [43, 44], increasing the CNT concentration to 1 wt% could have

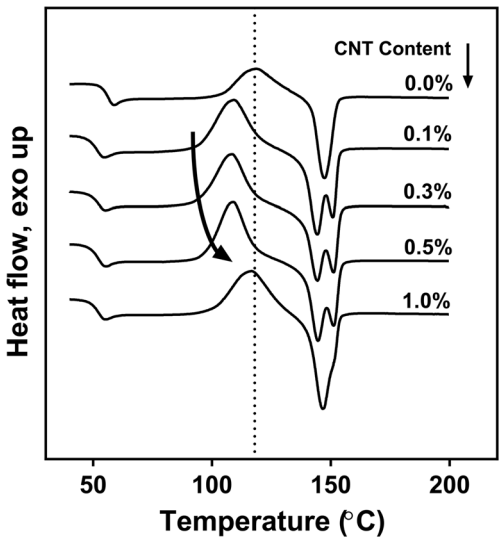

Fig. 2 DSC thermographs of the second heating cycle of PLA/CNT nanocomposites. The dashed line indicates T_{cc} of neat PLA (the concentration of CNTs is indicated next to each plot)

Table 2 DSC analysis of compounded PLA/CNT nanocomposites

CNTs Concentration (wt%)	T_g (°C)[b]	T_{cc} (°C)[b]	ΔH_c (J/g)[b]	Crystallinity (%)[a]	$T_{m,L}$ (°C)[b]	$T_{m,H}$ (°C)[a]
0.0	56.6 ± 0.8	118.5 ± 0.7	17.36 ± 1.21	2.81 ± 0.18	147.1 ± 0.8[c]	
0.1	51.7 ± 0.4	109.4 ± 0.6	26.75 ± 1.03	1.70 ± 0.43	144.3 ± 0.4	151.2 ± 0.7
0.3	52.0 ± 0.9	108.4 ± 1.1	24.95 ± 1.24	2.55 ± 0.84	144.3 ± 0.2	151.3 ± 0.1
0.5	52.6 ± 0.7	109.2 ± 0.6	26.13 ± 0.84	2.31 ± 0.31	144.5 ± 0.6	151.4 ± 0.2
1.0	52.8 ± 0.4	116.6 ± 0.8	25.78 ± 0.59	3.59 ± 0.67	146.7 ± 0.3	151.3 ± 0.5

[a] Calculated based on the first heating results

[b] Second heating cycle results

[c] Single melting peak value for neat PLA

Values are reported with the standard error

resulted in overwhelming of the recrystallization rate by the melting rate, which can be considered as the effect of higher CNT concentration on hindering the recrystallization during melting in relatively high heating rate of DSC measurements [44]. The peak *H* is observed as a small shoulder in the case of the 1-wt% CNT containing sample, indicating the reduced quantity of recrystallized phase during melting compared to the PLA/CNT nanocomposites with lower CNT content.

Data from the first heating cycle in DSC measurements were used for the calculation of the percent crystallinity of samples (Table 2). Although the second heating cycle is normally used as a reference point in studying the kinetics and degree of crystallization, it was critical to determine the crystallinity of each sample as is, before first heating without destroying their thermal history. In this respect, the effect of the original thermal history that each part undergoes during injection molding was taken into account for the calculation of the crystallinity of nanocomposites to establish a more accurate relationship between thermal and mechanical properties of as-prepared samples of different nanocomposites.

The images of the fracture surfaces of PLA/CNT nanocomposites are shown in Fig. 3. CNTs were mostly dispersed uniformly within the PLA matrix with some small agglomerations or bundles are present especially in the samples with higher CNT content. The formation of small agglomerations or bundles in nanocomposites with 0.5 and 1 wt% of CNTs were mostly due to the practical limitations of reaching to high levels of dispersity in melt compounding [30, 31]. A similar study by Patanwala et al. on 3D printing of PLA/CNT nanocomposites prepared by melt compounding reported the formation of CNT aggregates by increasing the concentration of CNTs without incorporation of any compatibilizers [28]. SEM images taken at higher magnifications showed that by increasing the CNTs content, the tendency of the CNTs to form bundles and aggregates was increased. This could be considered as a sign of weak filler-matrix interface which resulted in the formation of aggregates of CNTs in order to minimize the interface energy. SEM analysis of the fractured surfaces showed that increasing the CNT content resulted in rougher fracture surfaces, which could be attributed to the presence of more plastic deformation and higher energy absorption during deformation.

A uniform dispersion of CNTs plays a vital role in the crystallization of PLA matrix, as well as the mechanical reinforcement efficiency in nanocomposites. The tensile test results of injected molded neat PLA and PLA/CNT nanocomposites are presented in Fig. 4. The inclusion of CNTs within the PLA matrix resulted in minor enhancement of ultimate tensile strength (hereafter referred to as tensile strength) with a slight decrease in the yield strain. The nucleating role of CNTs for crystallinity development in PLA nanocomposites strongly depends on cooling rate and annealing [42]. Since the incorporation of CNTs at very low concentrations resulted in very slight changes in the crystallinity of nanocomposites prepared via injection molding, the induced reinforcing effect of CNTs was ascribed to the load transfer in a uniform state of dispersion within the PLA matrix with almost the same crystallinity in all nanocomposites. In this way, increasing the CNT content resulted in improved elastic modulus and tensile strength; however, the formation of agglomerations and bundles limited this improvement at higher CNT contents. Interestingly, the nanocomposites with 0.5-wt% CNTs, which showed lower crystallinity, also showed lower stiffness than other nanocomposites.

3.2 Thermal and mechanical characterization of 3D-printed nanocomposites

The thermo-physical and mechanical properties of the melt compounded nanocomposites were in compliance with the design and application requirements for the process of melt-extrusion AM [45, 46]. PLA/CNT nanocomposites prepared by twin-screw extrusion were 3D printed by a commercial desktop printer, and the thermal and mechanical properties of bulk nanocomposites were investigated for a better understanding of the performance of 3D-printed nanocomposites.

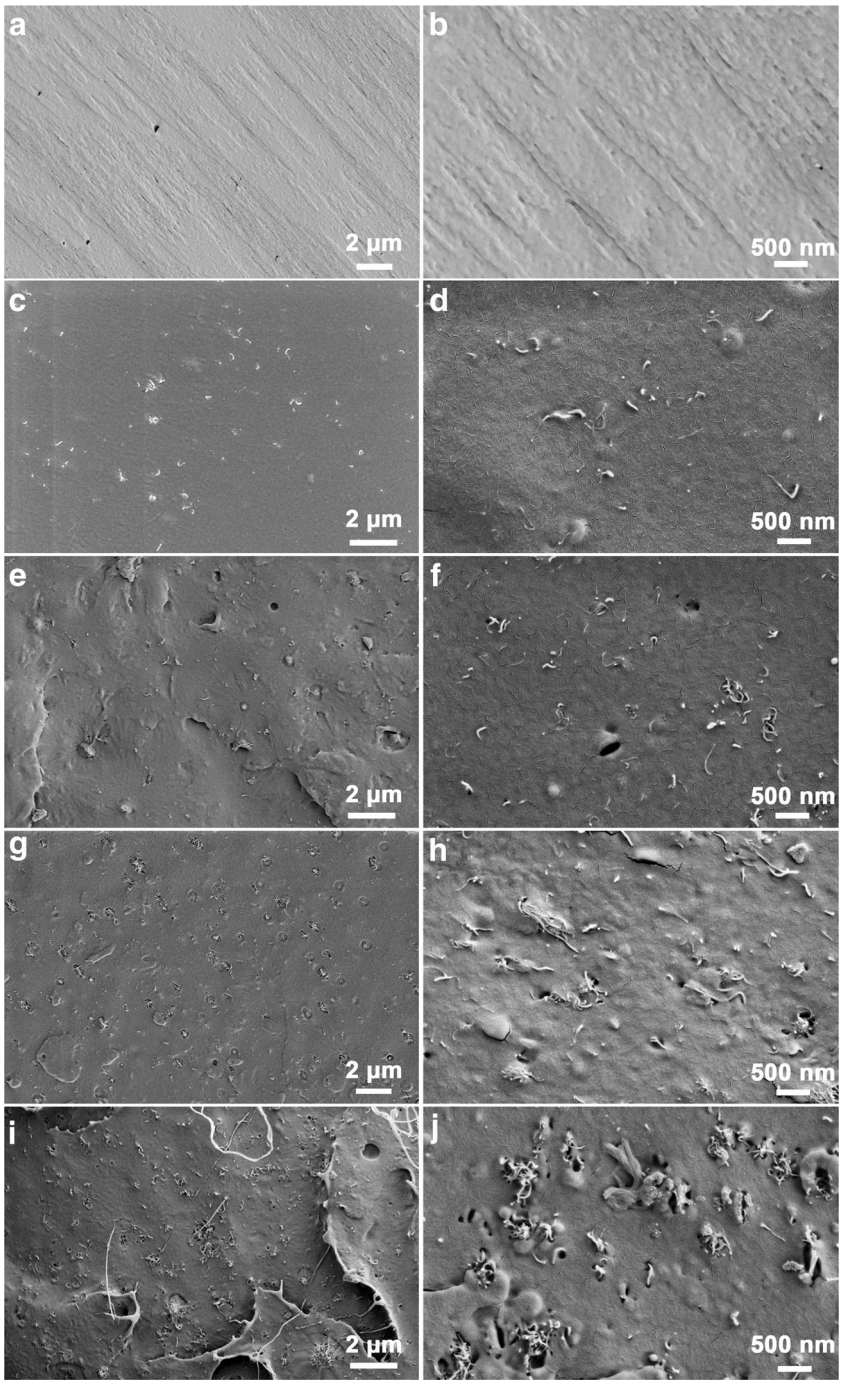

Fig. 3 SEM images of fracture surfaces showing the microstructure of neat PLA (**a**, **b**) and PLA/CNT nanocomposites with CNT concentration of 0.1 (**c**, **d**), 0.3 (**e**, **f**), 0.5 (**g**, **h**), and 1.0 wt.% (**i**, **j**)

Thermal properties of the PLA/CNT nanocomposites after 3D printing were analyzed by DSC to fully understand the effect of the thermal history induced by the heating regime during the printing process and the prolonged annealing time of parts during printing at temperatures above T_g. Figure 5 shows DSC thermographs of the 3D-printed samples (all were 3D printed according to design 2 in Table 1), and the corresponding values are given in Table 3. It has been previously shown that increasing the cooling rate will result in the vanishing of double melting behavior by decreasing the area under peak L and increasing the area under peak H [44]. Since the 3D-printed samples are cooled in a not-controlled manner, the observation of a single melting behavior during the first heating cycle of DSC measurements was expected, mainly due to the rapid cooling of the extrudates just after extrusion. This is in contrast with the controlled cooling rates applied during the first cooling cycle of DSC measurements, and hence the observed differences in melting behaviors in Figs. 2 and 5 would be expected. Interestingly, although the crystallinity of the injection molded and 3D-printed pure PLA samples was similar,

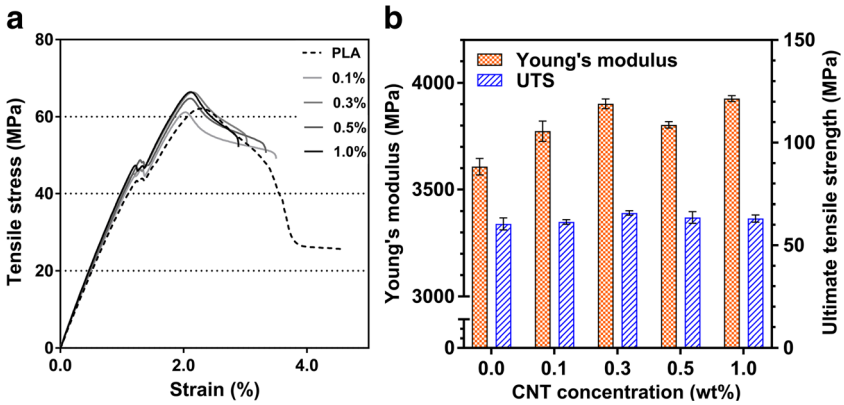

Fig. 4 Mechanical properties of PLA/CNT nanocomposites. **a** Representative stress-strain plots of dumbbell samples prepared by injection molding. **b** Young's modulus and tensile strength of nanocomposites. Error bars represent the standard errors

the crystallinity of PLA/CNT nanocomposites processed by 3D printing was significantly higher than same samples produced by injection molding, which was primarily due to strong dependency of crystallization kinetics of PLA nanocomposites on heating and cooling rates [42]. The similarity between the percent crystallinity of different nanocomposite samples can be attributed to the similarities between the thermal conditions during printing, namely, the layer thickness, build platform temperature, and the time of printing [47]. Since the reported data in Fig. 5 belong to samples produced with the same design, the observed crystallization behavior can be attributed to merely compositional factors. However, it was shown previously that changing the process parameters will affect the crystallization kinetics of 3D-printed PLA parts [47]. The results of the thermal characterization of 3D-printed samples presented herein can be considered as an index on how changing the CNT concentration will affect the kinetics of crystallization during similar manufacturing conditions, but for the possible interactions between process parameters and nanocomposite compositions, further complex designs of experiments would be required. It is important to note that the thermal processing conditions and the thermal history of 3D-printed parts were different from the injection molded parts. As a result, the 3D-printed nanocomposites showed a different crystallization behavior, as observed by DSC analysis, which consequently affected the mechanical properties of the 3D-printed parts. While T_{cc} was observed to be almost the same as neat PLA up to 0.5-wt% CNTs, a further increase in CNT content resulted in a significant decrease in $T_{cc.}$

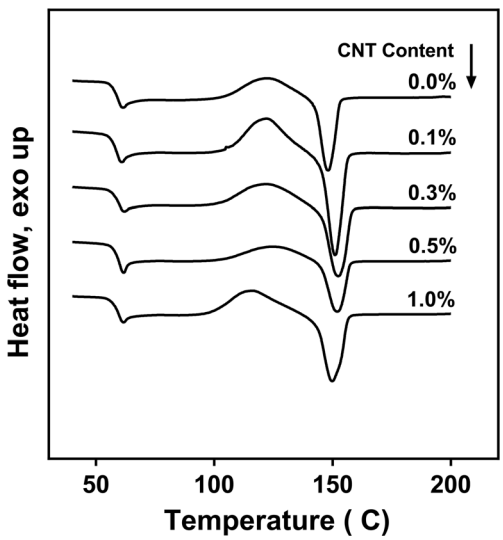

Fig. 5 DSC thermographs of 3D-printed nanocomposites from the first heating cycle (the concentration of CNTs is indicated next to each plot)

3.2.1 Tensile properties of 3D-printed nanocomposites

The tensile properties of 3D-printed nanocomposite samples with different building parameters are shown in Fig. 6. Three major building parameters, namely layer thickness, infill percentage, and infill pattern, were investigated and the corresponding results are presented in Fig. 5a–f, respectively.

The effect of the CNT content on the elastic modulus of each design was almost similar to the trend that was observed in the nanocomposite samples prepared by injection molding. The higher percent crystallinity due to thermal processing conditions of 3D-printed nanocomposites resulted in a higher order of elastic modulus improvement. A combined effect of increased crystallinity and reinforcing effect of CNTs by load transfer was pronounced in such property improvements. Moreover, an apparent decrease in the tensile strength of

Table 3 DSC analysis of PLA/CNT nanocomposites after 3D printing according to design 2 in Table 1 (all data from the first heating cycle)

CNTs concentration (wt%)	T_g (°C)	T_{cc} (°C)	Crystallinity (%)
0.0	59.3 ± 0.8	122.5 ± 0.3	2.97 ± 0.19
0.1	58.6 ± 0.4	120.1 ± 0.7	6.44 ± 0.46
0.3	59.5 ± 0.2	119.3 ± 1.1	6.68 ± 0.23
0.5	59.3 ± 0.7	122.3 ± 0.5	5.03 ± 0.71
1.0	59.1 ± 0.5	114.7 ± 0.9	6.49 ± 0.38

Values are reported with the standard error

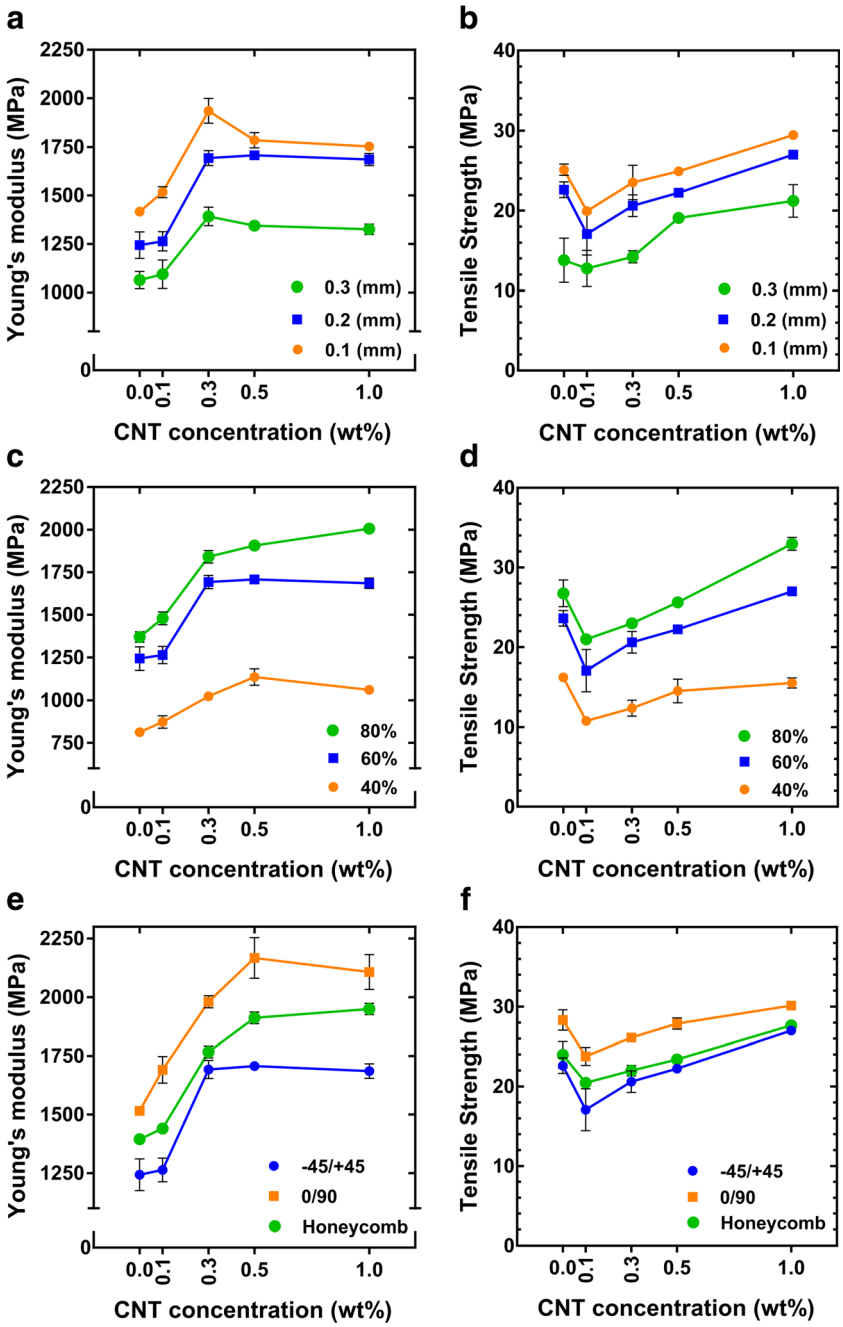

Fig. 6 Results of tensile testing for 3D-printed samples according to designs 1 to 7. Young's modulus and tensile strength are presented in three categories of building parameters, including layer thickness (**a**, **b**), infill percentage (**c**, **d**), and infill pattern (**e**, **f**). Error bars represent the standard errors

PLA/CNT nanocomposites compared to the samples of neat PLA was observed for all the investigated categories, which was previously reported in a few studies for bulk PLA/CNT nanocomposites [48–50]. This drop in tensile strength was interpreted as evidence for the presence of the CNT agglomerates, which influenced on early failure of small extruded strands within the 3D-printed structure. In this context, it should be noted that the state of dispersion of CNTs within PLA matrix would not be subjected to any noticeable changes within the experimental groups during 3D printing (i.e., by brief extrusion through a fine nozzle at a constant flow rate) [28]. Since the extruded strands have significantly small diameters, even presence of a few aggregates of CNTs can result in the formation of stress concentration regions and early failure of individual strands, which would subsequently result in early failure of the whole structure. However, CNT content of 3D-printed nanocomposites should not be considered as the sole major parameter affecting Young's modulus and tensile strength in each design category. The parameters, such as infill percentage (porosity), layer thickness (bonding between layers), and infill pattern (direction of load transfer), critically influence the stiffness of 3D-printed parts.

While all the 3D-printed parts showed similar trends in elastic modulus and tensile strengths as a function of the

CNT content as shown in Fig. 6a, b, both properties were found to decrease as a function of the layer thickness, while the infill density and raster direction were constant (Fig. 6a). The previous studies also reported similar results on the effect of layer thickness on stiffness and strength of 3D-printed plastics [3, 4, 10]. However, it should be noted that the infill density was set to be 100% in most of these previous studies. When the porosity and the gap between strands are varied, a porous 3D-printed structure is expected to have a different load transfer behavior than the fully dense one, due to less intra and trans-raster diffusion or integration of neighboring strands [33]. In this way, the applied load could be transferred through the trans-raster bonding regions. SEM was used to investigate the fractured surfaces of the 3D-printed nanocomposites according to designs 1 to 3 (Fig. 7), in which the layer thickness increased from 0.1 to 0.3 mm. With increasing layer thickness, the contact area of trans-raster bonding decreased, which led to lower modulus and tensile strength of the final printed parts [4]. The failure in the samples with lower layer thickness, and hence, larger trans-raster bonding regions tend to occur at sections closer to the bonding area and cracks were found to mostly develop at or near these regions. Considering the difference between the directions of the deformation and load transfer in + 45/− 45 criss-cross infill pattern, there seem to be more constraints in deformation of bonding regions (due to large bonding area) compared to the rest of strands within the same raster. Moreover, the higher the probability of occurrence of structural faults in those regions might induce crack formation and growth, which will eventually contribute to the fracture. Increased layer thickness resulted in early fracture of the samples, due to less number of available strands at a given cross-section for intra-raster load transfer and smaller trans-raster bonding regions. The same trend and pattern of failure due to the variation of layer thickness was observed by the incorporation of CNTs within the PLA matrix. However, by increasing the CNT content, the higher stiffness and strength of strands resulted in the occurrence of trans-raster bonding failure without the fracture of constitutive strands in the samples with large layer thickness.

The infill density has a considerable effect on the stiffness and mechanical strength of 3D-printed parts. The previous studies have reported that by increasing the porosity content, the mechanical properties of 3D-printed parts decline considerably and infill density was reported as one of the major parameters in determining the mechanical durability of 3D-printed parts [5, 11, 12]. As can be seen in Fig. 6c, a decrease in infill density from 80 to 40% resulted in almost 50% reduction of Young's modulus regardless of the CNTs content. However, the observed trend of reduction was not linear as the function of infill percentage, which was also reported by previous studies for different thermoplastics [5, 12]. A higher infill percentage, which meant a higher number of strands in a given cross-section, resulted in a better load transfer through the structure. The pattern of fracture changed from the development of cracks on individual fiber to at or near the trans-raster bonding regions by increasing the infill percentage. This transition caused energy absorbing development of cracks within the trans-raster bonding region in higher infill

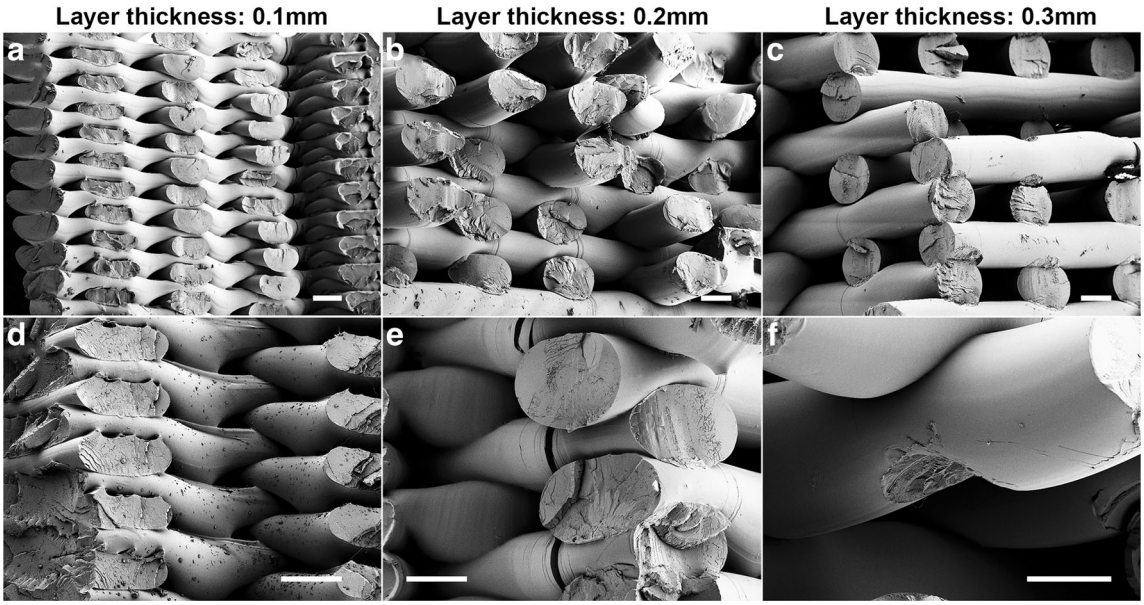

Fig. 7 Representative mesostructures and typical patterns of fracture in 3D-printed samples with different layer thickness values: 0.1 (**a**, **d**), 0.2 (**b**, **e**), and 0.3 mm (**c**, **f**). Images **d**, **e**, and **f** demonstrate how the fracture pattern changed from development of fracture at the trans-raster regions to failure of the individual fiber by increasing the layer thickness. Image **f** shows complete debonding at trans-raster region without formation of critical cracks. Top row images belong to PLA samples and the images presented in bottom row belong to nanocomposites with 0.3-wt% CNTs. All the images were taken from samples with + 45/− 45 infill pattern; scale bars: 200 μm

percentage which resulted in higher tensile strength. To highlight the combinatory effect of intra and trans-raster bonding and the infill density, an in-depth study by Patanwala et al. on the mutual interaction of over/under-filling conditions in the fabrication of fully dense parts with 3D printing is suggested to the reader [28]. Even though one might expect that by increasing the bonding regions (i.e., overfilling the mesostructure), the overall mechanical strength of the part should increase, but other factors such as the influence of higher flow rates on the alignment of CNTs might play an important role in load transfer and subsequent failure of the mesostructure. However, since all the experimental conditions in this paper are designed to have the same flow rate during extrusion, we have assumed that the variation between alignments of CNTs can be neglected from one design to another.

The effect of infill pattern (raster orientation) on the mechanical properties of plastics fabricated by 3D printing investigated in several studies [6, 7, 9, 11, 13, 51, 52]. The alignment of constitutive strands along the direction of loading determines the load transfer within the structure and its failure behavior. All previous studies have reported that changing the raster orientation from + 45/− 45 to 0/90 increases the stiffness and the strength of the part due to the alignment of constitutive strands with the direction of tensile loading, unless the process parameters are severely optimized to yield near to ideal conditions in terms of removal of residual structural voids [53]. As can be seen in Fig. 6e, f, the deviation from the loading direction resulted in the combination of tensile and shear loading conditions, which was in favor of early failure of the structures. On the other hand, the honeycomb pattern of infill had the load transfer characteristics of both + 45/− 45 and 0/90 infill patterns, by having path elements being both angled and parallel to the loading axis. This resulted in achieving tensile properties lying between those of two previously mentioned patterns. The SEM images of fracture surfaces of the 3D-printed nanocomposites according to designs 2, 6, and 7 are presented in Fig. 8. The fracture in samples with honeycomb infill pattern showed features similar to 0/90, similar in-plain failure of strands at the same cross-section despite their smaller number in a given unit of area. The partial alignment of extruder strands with the loading direction resulted in a significant enhancement of the stiffness of the 3D-printed nanocomposites, as well as a minor improvement of tensile strength, compared with the samples filled with the − 45/+ 45 criss-cross pattern. The less prominent enhancement of tensile strength compared to stiffness might be attributed to the higher probability of formation of structural faults due to large intra and trans-raster bonding regions, which resulted in an earlier fracture. However, honeycomb infill pattern can be considered as an alternative candidate to the 0/90 one in terms of achieving better tensile properties. Unlike its significant dependency on the direction of loading [8, 9, 54–56], it would be possible to provide more mechanical isotropicity in 3D-printed structures due to its in-plain symmetry along three axes.

3.3 Thermomechanical analysis of 3D-printed nanocomposites

Figure 9 shows the temperature dependency of dimensional change and coefficient of thermal expansion (CTE) in nanocomposites with 0.3-wt% CNTs. Since the scope of TMA in this study was to identify the influence of building parameters on the expansion behavior of 3D-printed nanocomposites, this section includes TMA results for only one composition with varying building parameters. The influence of building parameters in different design categories on the CTE in the z-axis direction (perpendicular to build plate) can be considered before and after glass transition temperature. The expansion behavior below T_g did not show significant dependency on the mesostructure and can be considered as the characteristic of the matrix material rather than being affected by the structural features. However, the expansion behavior of 3D-printed parts above T_g showed a strong dependency on the building parameters (dashed areas in Fig. 9). The effect of process parameters on the CTE of 3D-printed amorphous thermoplastics has been investigated in a few studies [57, 58]. According to previous reports, the thermal stress builds up during material extrusion; AM is one of the major causes resulting in anisotropic mechanical property development [58, 59]. Therefore, the building parameters are expected to have a significant influence on the accumulated thermal stress in 3D-printed parts, determined by the temperature of deposited thermoplastic, the cooling rate within the part, and the bonding regions between filaments. According to Fig. 9, a significant variation of

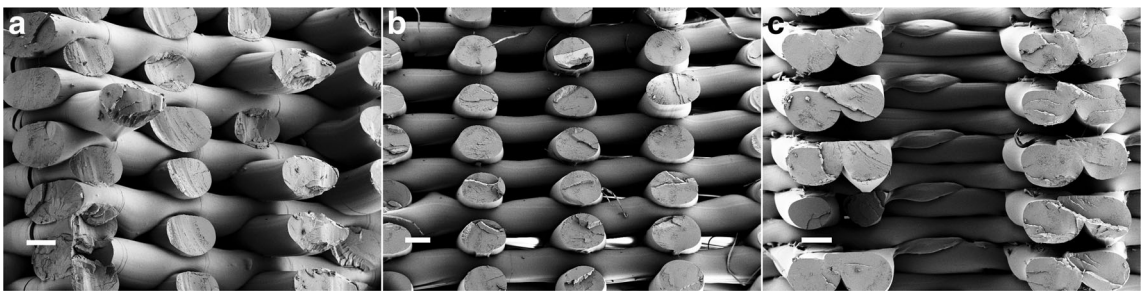

Fig. 8 Fracture surfaces of 3D-printed samples with different infill patterns: **a** − 45/+ 45 criss-cross, **b** 0/90, and **c** honeycomb; scale bars: 200 μm

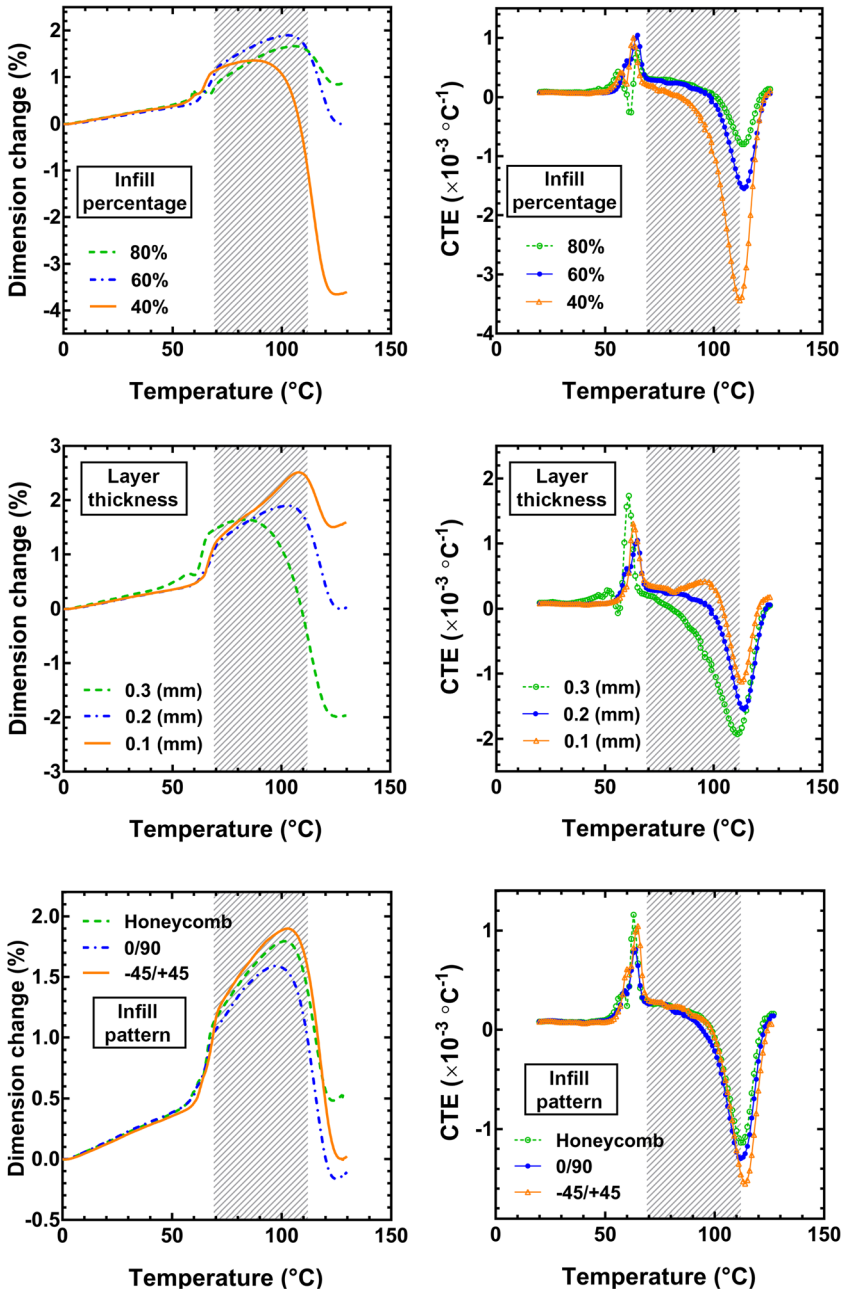

Fig. 9 Thermomechanical data are showing (left) dimensional change and (right) variation of CTE in nanocomposites with 0.3-wt% CNTs as a result of variation of building parameters. The shaded regions represent the temperature range between T_g and T_{cc}

dimensions upon heating above T_g was observed in all design categories. These variations, expansion of parts followed by contraction, can be attributed to mutual interaction and contribution of opposing factors: thermal expansion, cold crystallization of PLA/CNT nanocomposite, and the porosity content in the mesostructure. Just above T_g, the thermal expansion due to the increase in free volume is dominant, but the porosity content together with softening of polymer matrix resulted in decreased CTE upon further increase in temperature, followed by crystallization of nanocomposites, which induced a significant reduction of CTE and shrinkage of specimens in the z-direction. Infill percentage determines the porosity content of parts, and by assuming similar kinetic and behavior of cold crystallization in all samples, increasing the porosity content led to a drastic decrease in length and a much steeper CTE reduction. This assumption based on similar cold crystallization kinetics is only valid if we consider the same composition of nanocomposites, highlighting the effect of CNTs in crystallinity development of the PLA matrix. By increasing layer thickness from 0.1 to 0.3 mm, the area of trans-raster bonding regions decreased, which resulted in less thermal stress built up in 3D-printed samples and more mobile trans-raster regions [60]. This reduction of bonding area facilitates the porosity driven shrinkage in the z-direction. The data obtained from these two categories of designs suggest that the porosity content and the bonding regions between fillets (intra and trans-

raster) are two important factors determining the rate of CTE decrease upon heating, and the amount of shrinkage in the z-direction is directly proportional to the infill percentage and the inverse of the area of trans-raster bonding regions. Changing the infill pattern (raster orientation) resulted in a minor variation in the shrinkage of structures, but the honeycomb pattern showed a minimum change in the dimension. Since all the measurements were performed along the z-axis, not much variation in the dimensions due to changing the infill pattern at constant porosity and layer thickness were expected. However, a smaller dimensional change of the honeycomb pattern might be an indication of lower residual thermal stress induced during material extrusion AM process, which in turn would contribute to mechanically more isotropic behavior.

4 Conclusions

In this study, the effect of the changing of the mesostructure of 3D-printed PLA/CNT nanocomposites on the corresponding mechanical and thermal behaviors was investigated. Thermal processing conditions during 3D printing played a critical role in the crystallization behavior of PLA/CNT nanocomposites, and thus, the thermal history of the 3D-printed parts should be carefully considered in estimating corresponding mechanical properties. The TMA above the T_g of 3D-printed nanocomposites was used for indexing the residual thermal stresses. The higher dimensional change above T_g has been regarded as a measure of the residual stress build-up during 3D printing processes. The structure-property relationship in the 3D-printed nanocomposites was studied by changing the layer thickness, infill percentage, and the infill pattern. Increasing the layer thickness resulted in a significant decrease in mechanical properties and more porosity caused by shrinkage upon heating due to the formation of more mobile trans-raster bonding regions. On the other hand, increasing the infill percentage resulted in enhanced mechanical properties and less dimensional changes upon heating. Moreover, the observed pattern of dimensional changes caused by variation of infill percentage was strongly non-linear. The pattern of the infill played an important role in load transfer within the mesostructure. A honeycomb-shaped pattern was found to have higher thermal stability and mechanical properties compared to the conventional −45/+45 criss-cross pattern.

Funding information This research is supported by the Scientific and Technological Research Council of Turkey (TUBITAK) grant number 113M491.

References

1. Ian Campbell OD, Kowen J, Wohlers T (2018) 3D printing and additive manufacturing state of the industry. In: Annual Worldwide Progress report. Wohlers report. Wohlers Associates, Inc.
2. Dizon JRC, Espera AH, Chen Q, Advincula RC (2017) Mechanical characterization of 3D-printed polymers. Addit Manuf 20:44–67
3. Rankouhi B, Javadpour S, Delfanian F, Letcher T (2016) Failure analysis and mechanical characterization of 3D printed ABS with respect to layer thickness and orientation. J Fail Anal Prev 16(3): 467–481
4. Spoerk M, Arbeiter F, Cajner H, Sapkota J, Holzer C (2017) Parametric optimization of intra-and inter-layer strengths in parts produced by extrusion-based additive manufacturing of poly(lactic acid). J Appl Polym Sci 134(41)
5. Fernandez-Vicente M, Calle W, Ferrandiz S, Conejero A (2016) Effect of infill parameters on tensile mechanical behavior in desktop 3D printing. 3D Print Addit Manuf 3(3):183–192
6. Tymrak B, Kreiger M, Pearce JM (2014) Mechanical properties of components fabricated with open-source 3-D printers under realistic environmental conditions. Mater Des 58:242–246
7. Wu W, Geng P, Li G, Zhao D, Zhang H, Zhao J (2015) Influence of layer thickness and raster angle on the mechanical properties of 3D-printed PEEK and a comparative mechanical study between PEEK and ABS. Materials 8(9):5834–5846
8. Ahn S-H, Montero M, Odell D, Roundy S, Wright PK (2002) Anisotropic material properties of fused deposition modeling ABS. Rapid Prototyping J 8(4):248–257
9. Cantrell J, Rohde S, Damiani D, Gurnani R, DiSandro L, Anton J, Young A, Jerez A, Steinbach D, Kroese C (2017) Experimental characterization of the mechanical properties of 3D printed ABS and polycarbonate parts. In: Advancement of optical methods in experimental mechanics, volume 3. Springer, pp 89–105
10. Bayraktar Ö, Uzun G, Çakiroğlu R, Guldas A (2017) Experimental study on the 3D-printed plastic parts and predicting the mechanical properties using artificial neural networks. Polym Adv Technol 28(8):1044–1051
11. Mohamed OA, Mohamed OA, Masood SH, Masood SH, Bhowmik JL, Bhowmik JL (2017) Experimental investigation for dynamic stiffness and dimensional accuracy of FDM manufactured part using IV-optimal response surface design. Rapid Prototyping J 23(4):736–749
12. Baich L, Manogharan G, Marie H (2015) Study of infill print design on production cost-time of 3D printed ABS parts. Int J Rapid Manuf 5(3–4):308–319
13. Sood AK, Ohdar RK, Mahapatra SS (2010) Parametric appraisal of mechanical property of fused deposition modelling processed parts. Mater Des 31(1):287–295
14. Mohan N, Senthil P, Vinodh S, Jayanth N (2017) A review on composite materials and process parameters optimisation for the fused deposition modelling process. Virtual Phys Prototyp 12(1): 47–59
15. Kalsoom U, Nesterenko PN, Paull B (2016) Recent developments in 3D printable composite materials. RSC Adv 6(65):60355–60371
16. Dul S, Fambri L, Pegoretti A (2016) Fused deposition modelling with ABS–graphene nanocomposites. Compos A Appl Sci Manuf 85:181–191
17. Wei X, Li D, Jiang W, Gu Z, Wang X, Zhang Z, Sun Z (2015) 3D printable graphene composite. Sci Rep 5:11181
18. Singh R, Sandhu GS, Penna R, Farina I (2017) Investigations for thermal and electrical conductivity of ABS-graphene blended prototypes. Materials 10(8):881
19. Francis V, Jain PK (2016) Experimental investigations on fused deposition modelling of polymer-layered silicate nanocomposite. Virtual Phys Prototyp 11(2):109–121

20. Dorigato A, Moretti V, Dul S, Unterberger S, Pegoretti A (2017) Electrically conductive nanocomposites for fused deposition modelling. Synth Met 226:7–14
21. Gardner JM, Sauti G, Kim J-W, Cano RJ, Wincheski RA, Stelter CJ, Grimsley BW, Working DC, Siochi E (2016) 3-D printing of multifunctional carbon nanotube yarn reinforced components. Addit Manuf 12:38–44
22. Gnanasekaran K, Heijmans T, Van Bennekom S, Woldhuis H, Wijnia S, de With G, Friedrich H (2017) 3D printing of CNT-and graphene-based conductive polymer nanocomposites by fused deposition modeling. Appl Mater Today 9:21–28
23. Berretta S, Davies R, Shyng Y, Wang Y, Ghita O (2017) Fused deposition modelling of high temperature polymers: exploring CNT PEEK composites. Polym Test 63:251–262
24. Zhu D, Ren Y, Liao G, Jiang S, Liu F, Guo J, Xu G (2017) Thermal and mechanical properties of polyamide 12/graphene nanoplatelets nanocomposites and parts fabricated by fused deposition modeling. J Appl Polym Sci 134(39):45332
25. Zhang D, Chi B, Li B, Gao Z, Du Y, Guo J, Wei J (2016) Fabrication of highly conductive graphene flexible circuits by 3D printing. Synth Met 217:79–86
26. Bustillos J, Montero D, Nautiyal P, Loganathan A, Boesl B, Agarwal A (2017) Integration of graphene in poly (lactic) acid by 3D printing to develop creep and wear-resistant hierarchical nanocomposites. Polym Compos 149:100
27. Prashantha K, Roger F (2017) Multifunctional properties of 3D printed poly (lactic acid)/graphene nanocomposites by fused deposition modeling. J Macromol Sci A 54(1):24–29
28. Patanwala HS, Hong D, Vora SR, Bognet B, Ma AW (2018) The microstructure and mechanical properties of 3D printed carbon nanotube-polylactic acid composites. Polym Compos 39(S2): E1060–E1071
29. Lee C, Kim S, Kim H, Ahn S (2007) Measurement of anisotropic compressive strength of rapid prototyping parts. J Mater Process Technol 187:627–630
30. Raquez J-M, Habibi Y, Murariu M, Dubois P (2013) Polylactide (PLA)-based nanocomposites. Prog Polym Sci 38(10):1504–1542
31. Gonçalves C, Gonçalves IC, Magalhães FD, Pinto AM (2017) Poly(lactic acid) composites containing carbon-based nanomaterials: a review. Polymers 9(7):269
32. Sweeney CB, Lackey BA, Pospisil MJ, Achee TC, Hicks VK, Moran AG, Teipel BR, Saed MA, Green MJ (2017) Welding of 3D-printed carbon nanotube–polymer composites by locally induced microwave heating. Sci Adv 3(6):e1700262
33. Baich LJ (2016) Impact of infill design on mechanical strength and production cost in material extrusion based additive manufacturing. Youngstown State University
34. Alvarez C, Kenny L, Lagos C, Rodrigo F, Aizpun M (2016) Investigating the influence of infill percentage on the mechanical properties of fused deposition modelled ABS parts. Ingeniería e Investigación 36(3):110–116
35. Tsouknidas A, Pantazopoulos M, Katsoulis I, Fasnakis D, Maropoulos S, Michailidis N (2016) Impact absorption capacity of 3D-printed components fabricated by fused deposition modelling. Mater Des 102:41–44
36. Lužanin O, Movrin D, Plančak M (2014) Effect of layer thickness, deposition angle, and infill on maximum flexural force in FDM-built specimens. J Technol Plasticity 39(1):49–58
37. Carneiro OS, Silva A, Gomes R (2015) Fused deposition modeling with polypropylene. Mater Des 83:768–776
38. Vidović E, Faraguna F, Jukić A (2017) Influence of inorganic fillers on PLA crystallinity and thermal properties. J Therm Anal Calorim 127(1):371–380
39. Inkinen S, Hakkarainen M, Albertsson A-C, Södergård A (2011) From lactic acid to poly (lactic acid)(PLA): characterization and analysis of PLA and its precursors. Biomacromolecules 12(3): 523–532
40. Quan H, Zhang S-J, Qiao J-L, Zhang L-Y (2012) The electrical properties and crystallization of stereocomplex poly(lactic acid) filled with carbon nanotubes. Polymer 53(20):4547–4552
41. Bhattacharyya AR, Sreekumar T, Liu T, Kumar S, Ericson LM, Hauge RH, Smalley RE (2003) Crystallization and orientation studies in polypropylene/single wall carbon nanotube composite. Polymer 44(8):2373–2377
42. Saeidlou S, Huneault MA, Li H, Park CB (2012) Poly (lactic acid) crystallization. Prog Polym Sci 37(12):1657–1677
43. Wunderlich B (1980) Crystal melting. Academic Press
44. Yasuniwa M, Tsubakihara S, Sugimoto Y, Nakafuku C (2004) Thermal analysis of the double-melting behavior of poly (L-lactic acid). J Polym Sci B Polym Phys 42(1):25–32
45. Zhong W, Li F, Zhang Z, Song L, Li Z (2001) Short fiber reinforced composites for fused deposition modeling. Mater Sci Eng A 301(2): 125–130
46. Spoerk M, Savandaiah C, Arbeiter F, Sapkota J, Holzer C (2017) Optimization of mechanical properties of glass-spheres-filled polypropylene composites for extrusion-based additive manufacturing. Polym Compos
47. Wang L, Gramlich WM, Gardner D (2017) Improving the impact strength of poly(lactic acid)(PLA) in fused layer modeling (FLM). Polymer 114:242–248
48. Mat Desa M, Hassan A, Arsad A, Mohammad N (2014) Mechanical properties of poly (lactic acid)/multiwalled carbon nanotubes nanocomposites. Mater Res Innovations 18(sup6):S6–14–S16–17
49. Novais RM, Simon F, Pötschke P, Villmow T, Covas JA, Paiva MC (2013) Poly (lactic acid) composites with poly (lactic acid)-modified carbon nanotubes. J Polym Sci A Polym Chem 51(17):3740–3750
50. Moon SI, Jin F, Lee CJ, Tsutsumi S, Hyon SH (2005) Novel carbon nanotube/poly(L-lactic acid) nanocomposites; their modulus, thermal stability, and electrical conductivity. In: Macromolecular Symposia, vol 1. Wiley Online Library, pp 287–296
51. Ning F, Cong W, Hu Y, Wang H (2017) Additive manufacturing of carbon fiber-reinforced plastic composites using fused deposition modeling: effects of process parameters on tensile properties. J Compos Mater 51(4):451–462
52. Lanzotti A, Grasso M, Staiano G, Martorelli M (2015) The impact of process parameters on mechanical properties of parts fabricated in PLA with an open-source 3-D printer. Rapid Prototyping J 21(5): 604–617
53. Arbeiter F, Spoerk M, Wiener J, Gosch A, Pinter G (2018) Fracture mechanical characterization and lifetime estimation of near-homogeneous components produced by fused filament fabrication. Polym Test 66:105–113
54. Ziemian C, Sharma M, Ziemian S (2012) Anisotropic mechanical properties of ABS parts fabricated by fused deposition modelling. In: Mechanical engineering. InTech
55. Koch C, Van Hulle L, Rudolph N (2017) Investigation of mechanical anisotropy of the fused filament fabrication process via customized tool path generation. Addit Manuf
56. Zou R, Xia Y, Liu S, Hu P, Hou W, Hu Q, Shan C (2016) Isotropic and anisotropic elasticity and yielding of 3D printed material. Compos Part B Eng 99:506–513
57. Kantaros A, Karalekas D (2013) Fiber Bragg grating based investigation of residual strains in ABS parts fabricated by fused deposition modeling process. Mater Des 50:44–50
58. D'Amico AA, Debaie A, Peterson AM (2017) Effect of layer thickness on irreversible thermal expansion and interlayer strength in fused deposition modeling. Rapid Prototyping J (just-accepted): 00–00

59. Wang T-M, Xi J-T, Jin Y (2007) A model research for prototype warp deformation in the FDM process. Int J Adv Manuf Technol 33(11):1087–1096

60. Sun Q, Rizvi G, Bellehumeur C, Gu P (2008) Effect of processing conditions on the bonding quality of FDM polymer filaments. Rapid Prototyping J 14(2):72–80